JOURNAL OF GEOPHYSICAL RESEARCH, VOL. 97, NO. C2, PAGES 2391–2402, FEBRUARY 15, 1992

Identification of Sea Ice Types in Spaceborne Synthetic Aperture Radar Data

RONALD KWOK, ERIC RIGNOT, AND BENJAMIN HOLT

Jet Propulsion Laboratory, California Institute of Technology, Pasadena

R. ONSTOTT

Environmental Research Institute of Michigan, Ann Arbor

An approach for identification of sea ice types in spaceborne synthetic aperture radar (SAR) image data is presented. The unsupervised classification approach involves cluster analysis for segmentation of the image data followed by cluster labeling based on previously defined look-up tables containing the expected backscatter signatures of different ice types measured by land-based scatterometer. The particular look-up table used for labeling a segmented image is selected based on the seasonal and meteorological conditions at the time of data acquisition. The extensive scatterometer observations and experience accumulated in field campaigns during the last 10 years were used to construct these look-up tables. These tables are expected to evolve as sea ice observations from the European ERS-1 SAR become available. This paper presents the classification approach, its expected performance, the dependence of this performance on radar system performance, and expected ice scattering characteristics. Results using both aircraft and simulated ERS-1 SAR data are presented. The results are compared to limited field ice property measurements and coincident passive microwave imagery. An algorithm based on this experimental approach has been implemented in the geophysical processor system at the Alaska SAR Facility for classification of sea ice data in ERS-1 C band SAR data. The importance of an integrated postlaunch program for validation and improvement of this approach is discussed.

1. INTRODUCTION

The derivation of valuable information on sea ice properties from radar imagery has increased steadily over the last decade [*Carsey*, 1989]. As examples, studies utilizing synthetic aperture radar (SAR) imagery have examined the kinematics and deformation of the ice field [e.g., *Hall and Rothrock*, 1981; *Fily and Rothrock*, 1990; *Kwok et al.*, 1990], the comparison of active and passive microwave observations of concentration and ice types [e.g., *Burns et al.*, 1987; *Martin et al.*, 1987], the variability of ice properties that affect the atmospheric drag coefficient [*Burns*, 1990], and ice signatures. Investigations of the radar signatures of sea ice types using data from SAR and scatterometer systems have shown that radar backscatter varies with ice types as a result of differences in both internal (salinity and subsequent dielectric properties, density, inhomogeneities such as air bubbles) and surface properties (roughness, snow cover, distribution of water). The radar signatures vary with frequency, incidence angle, and polarization [e.g., *Ulaby et al.*, 1986; *Onstott et al.*, 1979, 1982; *Kim et al.*, 1985; *Livingstone and Drinkwater*, 1991; *Gray et al.*, 1982]. These ice properties also vary significantly with seasonal temperature variations [*Onstott and Gogineni*, 1985; *Onstott et al.*, 1987; *Holt and Digby*, 1985; *Livingstone et al.*, 1987*a*; *Carsey*, 1985; *Cavalieri et al.*, 1990] and by region [*Livingstone et al.*, 1987*b*]. Several recent studies have compared theoretical scattering models based on ice properties to the observed radar ice signatures [*Drinkwater et al.*, 1991; *Winebrenner et al.*, 1989; *Drinkwater*, 1989; *Kim et al.*, 1985]. Different image analysis approaches have been applied to the ice signatures to examine the types of information available in the SAR imagery for the automatic extraction of ice types [e.g., *Lyden et al.*, 1984; *Wackerman et al.*, 1988].

These SAR studies of sea ice have examined imagery obtained from aircraft and spaceborne SAR systems, usually in combination with other sensors, in situ measurements of ice and snow conditions, and near-surface scatterometer and radiometer measurements. The radars have operated over a wide range of frequencies, incidence angles, and polarizations. During this decade, single-channel spaceborne SARs are to be launched on the European ERS-1 in 1991, the Japanese ERS-1 in 1992, and the Canadian RADARSAT in 1994. These satellites will provide the first opportunities for the extensive spaceborne monitoring of the polar regions with a SAR since Seasat (which operated for $3\frac{1}{2}$ months in 1978). At the end of this decade, NASA has proposed to launch the EOS (Earth Observing System) SAR (a multifrequency, multipolarization SAR) as an integral component of the Mission to Planet Earth, a comprehensive suite of satellite instruments designed to examine global climate change, of which sea ice is a key and supposedly dramatic indicator.

In response to these opportunities for examining the polar regions with high-resolution, all-weather spaceborne SARs, the Alaska SAR Facility (ASF) has been implemented at the University of Alaska, Fairbanks, to receive, process, and archive SAR data from these satellites and to generate sea ice geophysical products from the data [*ASF Prelaunch Science Working Team*, 1989]. To generate these products, algorithms have been developed which will reside in a geophysical processor system (GPS) to automatically and routinely generate maps of ice motion [*Kwok et al.*, 1990],

Copyright 1992 by the American Geophysical Union.

Paper number 91JC02652.
0148-0227/92/91JC-02652$05.00

ocean surface wave direction and length [*Holt et al.*, 1990*a*] and ice type and concentration [*Holt et al.*, 1990*b*].

This paper focuses on the ice classification algorithm which has been implemented at ASF to generate these maps of ice type and concentration, first from ERS-1 and the evolution of such an algorithm with the introduction of ancillary data sets (such as passive microwave observations) and the upcoming JERS-1 and RADARSAT. The ASF GPS ice classification algorithm has been designed to efficiently segment the ice into the major ice types, including multiyear (MY) and first-year (FY) ice, by using a clustering routine to isolate their SAR ice signatures. The clusters are labeled (as ice types) by comparison with tables of scatterometer-derived ice type signatures that have been compiled by season. The algorithm will account for these seasonal changes by utilizing separate look-up tables. The development status of this classification algorithm has been reported previously by *Holt et al.* [1989, 1990*b*].

As was mentioned previously, the ice classification algorithm has been designed to be used with ERS-1 SAR imagery. The ERS-1 SAR is a single frequency (C band, 5.3 GHz), single polarization (vertical transmission and reception, or VV) radar with a fixed look angle of 23° off nadir. The satellite, launched on July 14, 1991, into a sun-synchronous orbit at 98° inclination, will acquire extensive imagery of sea ice over the Arctic Ocean and peripheral seas. On the basis of aircraft SAR imagery obtained at C band VV, the imagery from ERS-1 is expected to be extremely valuable for sea ice studies because of the high contrast in backscatter that exists between multiyear and first-year ice, particularly in the winter [*Cavalieri et al.*, 1991]. The GPS has been designed to take advantage of this brightness contrast.

The GPS will utilize reduced resolution (≈200 m) SAR data processed at the ASF. The low-resolution products are 8- by 8-pixel-averaged scenes made from four-look ground plane, full resolution (25 m) images and are 1024 by 1024 pixels in size. An advantage of using the lower-resolution image products is the low level of multiplicative noise or speckle that is present after the averaging process. Thus it is possible to avoid special segmentation techniques [*Lyden*, 1984; *Wackerman et al.*, 1988] which account for speckle statistics to minimize classification errors. This simplifies the task of the automated procedure to finding optimum thresholds for segmentation of the different ice types using the expected microwave responses at C band. The current algorithm is based entirely on mean backscatter coefficients and does not attempt to exploit the two-dimensional or statistical structure (e.g., texture, higher-order moments, etc.) of specific ice types. Although these features have been shown to be effective in some cases, there are insufficient observations at this time to support the implementation of such feature extraction schemes in an operational system.

The seasonal evolution of the active microwave responses of sea ice are described in the work of Onstott and coworkers [*Onstott et al.*, 1979, 1982, 1987; *Onstott and Gogineni*, 1985; *Onstott and Shuchman*, 1988]. Preliminary assessment and comparison of SAR data with scatterometer data at C-band showed that there is a consistent contrast (of 5–6 dB) between MY and FY ice during winter conditions, which serves as an important discrimination feature. In the summer, scatterometer measurements [*Onstott et al.*, 1987; *Onstott and Gogineni*, 1985] have shown that reductions and even reversals in this contrast have been observed during warm, melt conditions due to changes in scattering characteristics caused by changes in surface conditions of the ice and snow cover. In this regime, the contrast between ice and water is still available for separation of the two classes for ice concentration calculations. Perhaps the most difficult time periods to evaluate are the seasonal transitions (spring and fall), when the most dramatic changes in the microwave backscatter from the ice are expected. The present plan is to implement a classification procedure for seasons when the surface conditions remain fairly stable and a high confidence can be placed on the classification results. Validation and extension of the procedure to other seasons and conditions is dependent on routine SAR observations from ERS-1 as well as correlative data (e.g., surface measurements) for adapting the classifier to these datasets. A significant factor affecting the number of ice types that can be effectively discriminated is the performance of the radar sensor and processing system. The percentage misclassification is directly dependent on the relative as well as absolute calibration of the sensor.

In this paper we will examine the factors which affect the performance of the classification system: (1) system factors (radar sensor and processing system performance), (2) internal factors (classifier parameters), and (3) external factors (seasonal variations in backscatter signatures). The next section presents the classification procedure with a discussion of each element in the algorithm flow. Section 3 summarizes the simulation procedure and the dataset used for evaluation of the classification products. Results and observations are included in section 4. Finally, the key observations are presented with a brief discussion of the importance of an integrated effort required to validate the performance and quality of such an algorithm.

2. Classification Approach

This section provides a description and analysis of each of the elements within the algorithm flow. The flow diagram of the classification procedure is shown in Figure 1. The three subsections describe the major components and processes of the classification scheme: (1) radar data calibration, (2) image segmentation and labeling, and (3) the critical look-up tables used to label the ice type of individual pixels. These subsections represent logical grouping of the topics rather than the order in which they appear in Figure 1.

2.1. *Radar Data Calibration*

Data calibration. Since this is an unsupervised intensity-based classification procedure, the labeling of individual pixels is dependent on the overall system calibration. In the case of the radar system, pixel values are mapped into their corresponding backscatter coefficients. The process of calibration involves two steps: (1) the removal of the system noise bias to the digital sample, and (2) the mapping of the resultant value into a backscatter coefficient. The data required for calibration is available from the processing table associated with each image frame produced by the ASF systems. This table establishes the proportionality between the pixel values and the backscatter coefficients, σ_0. The sensitivity of the classification procedure to the accuracy of the data calibration is discussed in the following sections.

Residual antenna pattern correction. Incorrect compensation of the antenna pattern in SAR image data (causing

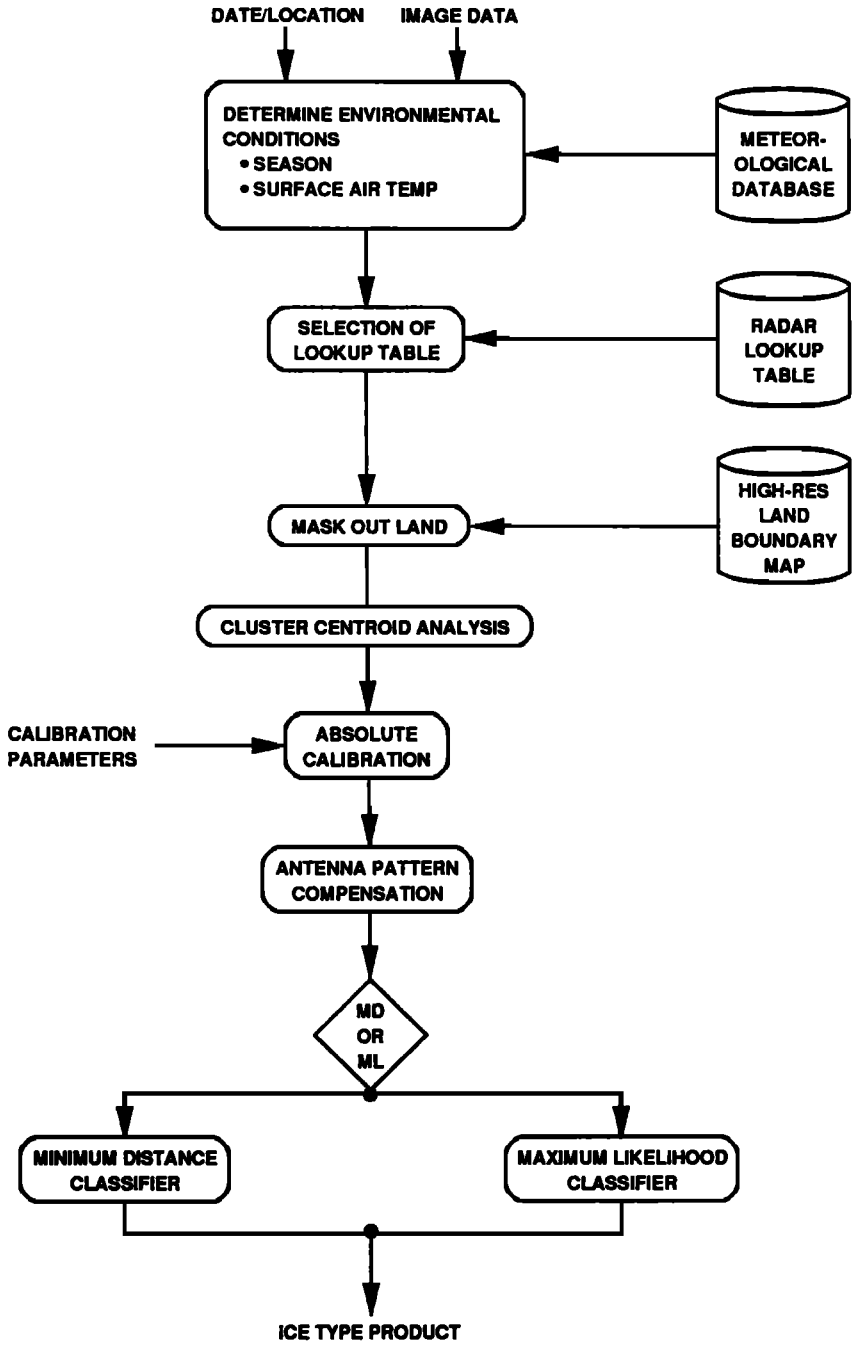

Fig. 1. Sea ice classification approach.

range intensity gradients) is frequently a problem when there are uncertainties in antenna pointing and preflight pattern measurements. Even though the ERS-1 antenna gain pattern approximates that of a ramp (which takes into account the expected R^3 range dependence), thus reducing the sensitivity to pointing errors, residuals could still occur. Here the residuals are modeled as a linear ramp; however, higher-order polynomials could be used if postlaunch measurements indicate such strategy is necessary. To estimate the parameters of the linear error model, 16 windows of 100 by 100 pixels each uniformly distributed within the image frame are selected for cluster analysis. The dominant bright clusters identified at each window location are selected, and the ones not within the tolerance of the expected residuals are discarded. The remaining cluster centroids are then used for regression analysis to determine the parameters (slope) of the linear model. The simulation results for four cases are shown in Table 1. The ramp is measured before and after the addition of a 1-dB range ramp. On the basis of the results, the procedure can determine a linear ramp to approximately 0.5-dB accuracy. This step will also remove any natural incidence angle–dependent variations of sea ice (approximately 0.5 dB across the range of FRS-1 for multiyear ice) in the backscatter cross sections as well. The expected response at the center of the image is used as a reference. Thus, the relative calibration (consistency in the pixel value of the same ice type within an image frame) requirements of the pixel samples can be relaxed.

TABLE 1. Performance of Estimation of a 1-dB Ramp

Image	Ramp, dB: Original Image	Ramp, dB: Estimated	Expected Ramp, dB	Error, dB
1	0.54	1.05	1.54	0.49
2	−0.1	0.46	0.9	0.44
3	−0.36	0.15	0.64	0.49
4	−0.84	0.18	0.16	−0.02

2.2. *Image Segmentation and Labeling*

Cluster analysis. This step is used to identify the dominant or reference (cluster with the largest sample population) cluster within the image frame with the goal of labeling this cluster as an ice type in the next step of the procedure. Clustering is performed in the intensity domain and not in the normalized logarithm representation. The selection of the dominant cluster is to insure that the mean backscatter of that ice type is reasonably estimated. For example, this step would avoid selection of the cluster which is dominated by brighter ridge pixels from a smaller population. An efficient cluster analysis technique called ISODATA is used to identify the natural intensity clusters. This iterative technique is characterized by the addition of heuristics to group, eliminate, and/or split clusters on the basis of parameters specified by the user. The input parameters for clustering are simply the desired number of classes and the expected within-class scatter and between-class scatter. This method is based on the minimization of the sum of squared Euclidean distance between the sample and cluster center. A detailed description of ISODATA is given by *Ball and Hall* [1967] and *Tou and Gonzalez* [1974]. The technique assumes that the user has a certain degree of familiarity with the data for optimal performance. As stated earlier, the knowledge of the significant contrast between FY and MY ice in winter C band VV data has been incorporated into our scheme for mechanizing this unsupervised clustering technique. Tests have shown that only a small subset of the image (3 to 5% in area) is needed to obtain stable clustering results, i.e., cluster centroids vary little after a sufficient number of pixels representative of the ice types in the image are sampled. The rationale for choosing a small sample population is that the clustering procedure becomes inefficient as the sample population increases in size, which is due to the number of distance computations per iteration. Uniformly distributed data samples are selected for cluster analysis. An ice type with small areal extent would obviously not contribute to the analysis, but small populations will be accounted for later when individual pixels are labeled. Sensitivity studies based on varying the clustering parameters (using available data) have shown that this technique can consistently locate the cluster centroids to within 0.5 dB.

Cluster labeling. The backscatter value of the centroid of the dominant cluster does not necessarily correspond to a reference backscatter coefficient of an ice type stored in a look-up table (see section 2.3). The cluster is labeled as belonging to that ice type with the backscatter coefficient closest (absolute distance) to that in the look-up table. This is equivalent to identification of an radiometric tie point when there exists a radiometric misregistration between the measured and expected measurements. This uncertainty in data calibration should be less than the expected separation of the ice types, or else there could be ambiguity in the labeling procedure. For example, if the contrast between FY and MY ice is 5 dB, then the absolute calibration (consistency in the estimated cross section between one image frame and another) accuracy should be better than ±2.5 dB to avoid this labeling ambiguity.

Location of other ice types. The centroids of all the other ice types are located by using the expected contrast between different ice types stored in the look-up table. For example, if MY ice is identified as the reference cluster, then the relative locations of the other ice types i are

$$R^i_{\mathrm{MY}} = \frac{\sigma_i}{\sigma_{\mathrm{MY}}}$$

This step locates the small populations within the image which were omitted in the cluster analysis. This approach assumes certain amount of stability in the separation between the backscatter responses of different ice types. One factor that should be considered is the effect of uncompensated system noise bias which would shift the relative location of the ice types in the intensity histogram relative to the reference cluster,

$$R^i_{\mathrm{MY}} = \frac{\sigma_i + n}{\sigma_{\mathrm{MY}} + n}$$

Here the effect of the uncompensated system noise power n is a mislocation of the ice types which affects the final classification accuracy.

Pixel labeling. The final step is to give each image pixel an ice type label. Two alternative methods for pixel classification are: minimum distance and Bayes. The first is a simple one-dimensional thresholding of the intensity values based on the cluster locations C_i, where

$$x \sim C_i \qquad |x - C_i| = \text{minimum}$$

where x is the backscatter value, and $\sim$ is the assignment operator. The second is a more optimal approach if there are large differences in the expected natural variability of the different ice types. Simply,

$$x \sim C_i \qquad P(C_i)p(x/C_i) = \text{maximum}$$

The advantage of this method is that it accounts for differences in the density functions. For example, if the FY ice has a larger variance than MY ice, then the error rate would be minimized if such an approach is taken. The disadvantage of the Bayes approach is that the distribution densities $p(x/C_i)$ and the a priori probabilities $P(C_i)$ of the ice types as well as parameters describing their distributions have to be estimated. Also, the spatial and temporal dependence of these statistical parameters is probably quite high (owing to snow cover, ice deformation and surface temperature variations), and therefore the use of this technique is difficult to evaluate. However, both classifiers will be available to the user in the operational system. Only the minimum distance classifier has been evaluated thus far.

Additionally, we expect the observed variability of an ice type to be more dependent on resolution than the mean backscatter. The location uncertainty of the cluster centroid during cluster analysis (0.5 dB as pointed out earlier) obviously affects classification accuracy. The sensitivity is analyzed by varying the centroid location about a reference point and assessing the percentage of misclassified pixels.

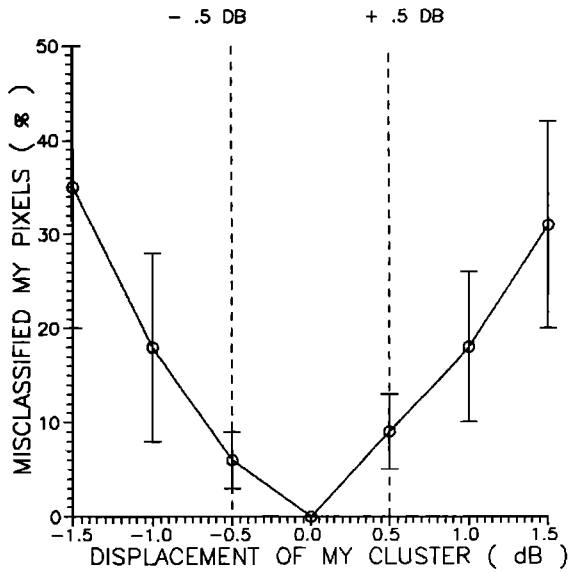

Fig. 2. Sensitivity of classifier: dependence of classification accuracy on errors in the location of the cluster centroids.

Figure 2 shows the percentage of misclassified pixels as a function of the uncertainty in the location of the cluster centroid. The results based on evaluation of four aircraft images showed that we can expect a 5% to 10% error given the 0.5-dB uncertainty in the location of the cluster centroids. It should be noted that this analysis considered only the classifier parameters and excluded all the other factors which might affect classification accuracy. These errors are acceptable for many sea ice studies [*ASF Prelaunch Science Working Team*, 1989]. For example, the ambiguity between deformed FY and MY ice (i.e., in that thickness regime) would have very little effect on regional flux calculations.

2.3. *Look-up Tables: Description*

The design of the scatterometer-derived look-up tables used in the ice type labeling process is described here. Each individual ice type and its associated backscatter coefficient are included in each of these tables. The dependence of the backscatter signature of the principal ice types on season and environmental conditions are coded in different look-up tables. Table 2 illustrates the conditions for selecting the different look-up tables as well as the principal ice types which are likely to be discriminable based on these conditions. This table serves as a basis for further improvements as ERS-1 data become available. It is anticipated that an extensive data base will be constructed that will enable better quantification and characterization of the spatial, temporal, and meteorological dependence of the microwave signatures of sea ice. It is important to note that the goal, based on our current knowledge, is not only to identify all the conditions and factors which affect these look-up tables but also to identify conditions when different approaches to ice classification have to be considered. Some of the knowledge incorporated into the current set of look-up tables is described below.

Seasonal dependence and transitions. The general time spans of the different "seasons" listed in the Table 2 are based on the climatology of sea ice. The actual timing of the transitional periods will be narrowed down by evaluating the correlations between local meteorological conditions and backscatter responses of the ice, a task that will be undertaken when routine ERS-1 observations become available. The initial validation effort will focus on the performance of the classifier under winter Arctic conditions using data processed at the ASF. Sea ice undergoes seasonal transitions from the winter, when growth and snow accumulation occur; through the spring period of snow and ice surface melting and refreezing; into the summer period, when extensive snow and ice melt forms ponds which eventually drain; and finally into fall, when the temperatures drop and ice growth and snowfall begins. These seasonal cycles are distinguishable in active microwave data and have distinct signatures (see *Onstott et al.* [1987] for overview).

The look-up tables. There are a total of six look-up tables (winter to early spring, late spring, early summer, midsummer, late summer, and fall; Table 3) corresponding to the time spans which have definitive characteristics relative to microwave responses of sea ice. The range of thickness, the normalized backscatter coefficient, the natural variability, and the incidence angle behavior of the principal ice types are shown in these tables. The ice types with backscatter coefficients below the system noise performance of −18 dB are indicated in the table. As was mentioned before, the backscatter signatures in the look-up tables are based on scatterometer measurements. Only the best available calibrated scatterometer measurements were included. An ice type with a specific backscatter signature has been verified with in situ measurements of the physical properties, and the environmental conditions during which the measurements were taken have been well documented. Entries in the look-up tables represent years of observations and experience acquired during field campaigns and are based extensively on the work of *Onstott et al.* [1979, 1982, 1987] and

TABLE 2. Seasonal and Temperature Dependence of Active Microwave Sea Ice Signatures at C Band VV

Season	General Time Span	Climatology Ambient Temperature	Principal Ice Types*
Winter to early spring	Oct.–May	$T < -10°C$	MY, FY, NI/OW
Late spring	May–June	$-10°C < T < 0°C$	ice, water
Early summer	June	$T \simeq 0°C$	ice, water
Midsummer	July	$T \geq 0°C$	ice, water
Late summer	August	$T \geq 0°C$	ice, water
Fall	Sept.–Oct.	$-10°C < T < 0°C$	MY, FY, NI/OW

*Ice types that are most likely to be separable in C-VV ERS-1 data. Abbreviations are MY, multiyear ice; FY; first-year ice; NI/OW, new ice/smooth open water.

TABLE 3. Seasonal Dependent Scatterometer-Derived Backscatter (C Band VV at 25° Incidence) Look-up Tables for Classification of Sea Ice Types in SAR Data

Ice Type	Thickness, cm	σ_0, dB	STD, dB	Slope, dB
		Winter to Early Spring		
MY	>220	−8.6	2.2	−0.08
FY	20–220	−14.0	2.1	−0.24
NI/OW	0–20	<−18	···	···
		Late Spring		
MY	>220	−10.7	2.1	−0.27
FY	70–220	−13.2	1.1	−0.22
NI/OW	0–20	<−18.0	···	···
		Early Summer, Midsummer, Late Summer		
MY/FY	>20	>−16.0	···	···
NI/OW	0–20	<−18.0	···	···
		Fall		
MY	>150	−10.5	1.7	−0.04
FY	30–120	−12.5	1.9	−0.21
NI/OW	0–30	<−18.0	···	···

The columns indicate ice types, ice thickness, normalized backscatter cross section, standard deviation of the backscatter, and the expected incidence angle dependence of the backscatter. (There are gaps where no scatterometer measurements are available in certain thickness ranges). Ice types are MY, multiyear; FY, thick first-year; NI/OW, new ice/smooth open water.

Onstott and Gogenini [1985]. Because of the disparity in the resolution of the scatterometer observations and the SAR measurements, it is expected that the SAR backscatter measurements will be modulated to a higher degree by mixture distributions (of ice types) compared with scatterometer samples. Comparison of the DC-8 SAR measurements and the scatterometer winter look-up table showed the mean backscatter and the separation between ice types to be similar (section 4). We anticipate that the mixture distribution of ice types will tend to affect the expected variability more than the mean statistic. The actual pixel classifier (minimum distance versus Bayes) which will be utilized in the algorithm will be based on these results.

Effect of wind. The normalized radar cross section of open water is dependent on wind speed and direction. Currently, we do not have a strategy for classification of open water with its varying radar cross section. The limited fetch of leads may also result in significant backscatter variability within a single lead. The classification products will indicate the wind velocity at the time of data acquisition. Wind velocity and air temperature fields (discussed below) used in the algorithm will be extracted from the numerical data products distributed by the National Meterological Center (NMC). These analyzed NMC fields are available twice (0000 UT and 1200 UT) daily.

Air temperature. The scattering characteristics of sea ice are highly dependent on air temperature. If the ice surface temperature (in response to air temperature) rises to a point where significant moisture in the ice from melt increases the complex dielectric constant, the sea ice response would cause ambiguity in the classification. It is obvious that the availability of air temperature measurements would help in identifying such conditions. The accuracy of the NMC temperature fields in the Arctic is currently being investigated (R. Colony, personal communication, 1991).

Effectively, the look-up table selected to classify a specific image will be a function of the season and ambient air temperature. To account for all the possible conditions, the decision table shown in Table 4 will be used. It is apparent that other factors (surface air pressure, geographic location, etc.) could be used in the decision table, and the software system which will be implemented will have the capability for future enhancement of this decision table based on available ancillary data. For example, passive microwave data could potentially be used synergistically with backscatter data for achieving a more precise identification of seasonal change, and therefore more accurate sea ice classification would result from the SAR imagery.

3. Data Set and Simulation

Data set. For realistic evaluation of the classification scheme, simulated ERS-1 image data approximating the expected quality of that processed at the ASF were generated. The NASA Jet Propulsion Laboratory (JPL) DC-8 SAR C band VV high-resolution data were used to generate four-look square-root intensity imagery of sea ice of sizes 1024 by 750 azimuth and range samples, respectively. The set of aircraft SAR imagery used in the algorithm evaluation was acquired during the March 1988 NASA DC-8 special sensor microwave imager (SSM/I) algorithm validation program [*Cavalieri et al.*, 1991]. That dataset provided extensive data from the Alaskan Beaufort, Chukchi, and Bering seas. The aircraft SAR, designed and built at JPL, operates at C, L, and P bands with quad-polarization capability. Only the C-band VV data were used here. Another data set available, used here mainly for verification of the classification procedure, is from the K_a band scanning imaging radiometer (KRMS) operated on a Navy P-3 aircraft [*Eppler et al.*, 1986] that was flown coincidentally with the NASA DC-8.

Data simulation. To simulate the ASF ERS-1 image product which will be used in the classification scheme, the four-look aircraft data were convolved with an 8 by 8 box filter which is identical to the procedure used to generate the low-resolution (100-m pixel spacing) imagery at ASF. The key differences between the aircraft and ERS-1 data are shown in Table 5. The noise-equivalent normalized cross section $NE\sigma_0$ (or the equivalent cross-section of the system noise level), approximately −30 dB in the aircraft data, is considerably better than the ERS-1's expected performance of −18 dB, so additional noise power was introduced (before the averaging process) in the aircraft data to more closely simulate the ERS-1 data. This effectively reduces our ability to detect ice types with backscatter coefficients less than −18 dB. Based on the backscatter coefficient of multiyear ice, typically −9 dB at C band VV, a noise level was added such that the expected signal-to-noise ratio of multiyear

TABLE 4. Algorithm Decision Table

Ambient Temperature	Winter	LSp	ES	MS	LS	Fall
$T < -10°C$	1	1	2	4	5	6
$-10°C < T < 0°C$	1	2	2	4	5	6
$T \geq 0°C$	1	2	3	4	5	5

Numbers denotes tables as follows: 1, Winter to spring look-up table; 2, late spring (LSp) look-up table; 3, early summer (ES) look-up table; 4, midsummer (MS) look-up table; 5, late summer (LS) look-up table; 6, fall look-up table.

pixel samples was degraded to 9 dB (for an NEσ_0 of −18 dB) and accordingly for the other ice types. The SAR image model used for this simulation is

$$I = (\mu + \eta)F_N$$

Here, I is the image intensity, μ is the mean backscatter power, η is the total system noise power contribution, F_N is the fading random variable which modulates the expected backscatter, and N is the number of looks of a SAR pixel sample. The fading modulation is a consequence of the coherent nature of the imaging system and is caused by the interference of the various scatterers within the resolution element. It is characterized by a chi-square distribution with $2N$ degrees of freedom [*Ulaby et al.*, 1986]. The incidence angle diversity in the aircraft data is much higher than that of ERS-1; hence only the near-range swath (with incidence angles between 23° and 38°) of the aircraft imagery is used.

A distinct bimodal histogram of the simulated SAR data can be observed in Figure 3, a result of the spatial averaging of the data which suppresses the fading modulation of the signal. There is significant separation between multiyear and first-year ice, and the next section describes how the automated approach exploits this contrast in the two ice types.

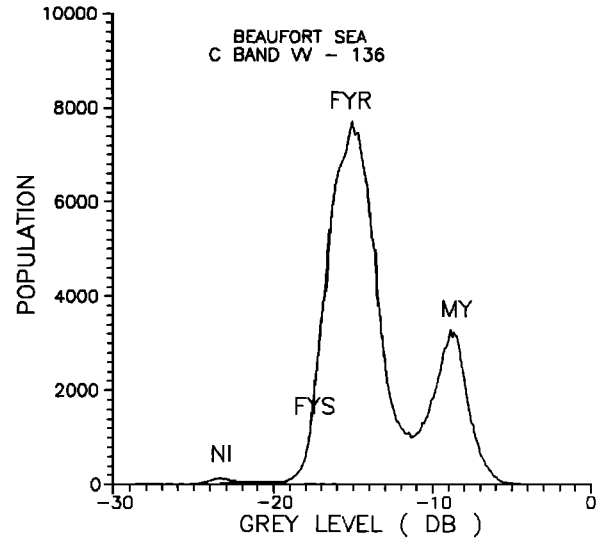

Fig. 3. Example histogram of a simulated ERS-1 64-look sea ice image. The peaks of the different ice types are well separated (MY, multi-year ice; FYR, rough deformed first-year ice; FYS, smooth first-year ice; NI, new ice/open water).

4. Results

This section shows results of sample simulations and comparison of the aircraft imagery with KRMS and the limited surface measurements obtained from a field camp that was overflown by the DC-8 during March 1988.

Classification of the modified DC-8 data. Plate 1 shows a sample DC-8 image with the image quality (noise floor, number of looks) modified to simulate the low-resolution (100-m pixel spacing) ERS-1 data generated at the Alaska SAR Facility. The incidence angle range within the strip is 20°–38°. The C band VV data were acquired in the central Beaufort Sea on March 11, when the air temperature was below −10°C. Based on the season and the conditions, the particular look-up table selected for the classification procedure was the winter look-up table (top section of Table 3). The contrast between the MY and FY ice was approximately 5 dB, similar to that predicted by the scatterometer measurements in the look-up table. The ice type map generated by the classification scheme is shown in Plate 1, indicating that the MY and FY ice are correctly classified (on the basis of visual classification of the image frame). The region that is coded in red has a very low backscatter cross section (less than −18 dB) which is indicative of new ice or open water and which is close to the noise floor of the sensor. The principal thick ice types could be easily separated within these images. Such is also the case for tests with aircraft SAR images (from the NASA DC-8) from the Chukchi Sea as well. A total of 10 SAR images from the Beaufort and Chukchi seas were classified and evaluated. This classification procedure has not been evaluated with C band VV SAR image data from other seasons owing to the lack of availability of SAR data from these seasons.

TABLE 5. Differences Between the Image Quality of the Low-Resolution ASF ERS-1 Data and the JPL DC-8 C Band VV Data

	Low-Resolution E-ERS-1	DC-8 C Band VV
Number of looks	8 × 8 averaged from four-looks	4-look
Resolution (ground range) m	100–200	12 × 18
Noise equivalent σ_0, dB	−18	−30
Look angle,* deg	20–26	20–60
Swath width, km	100	7–10

*The aircraft data collected in the 20–38° range were used in the algorithm evaluations.

Comparison of field camp ice and environmental observations with aircraft SAR imagery. An overflight of an ice camp in the Beaufort Sea was made on March 19, 1988. The ice camp was located approximately 350 km north of Prudhoe Bay and supported underwater acoustic propagation studies [*Wen et al.*, 1989]. The camp was located on the edge of a multiyear floe, adjacent to a refrozen lead which served as an aircraft landing strip.

The environmental and ice data that were collected provide the only known surface information obtained during the period of the aircraft campaign and confirm the winter conditions and the identification of FY and MY ice in the imagery. The environmental conditions were monitored at semiregular intervals at the camp (Figure 4). From March 11 to March 19, the dates of the aircraft flights in the Beaufort and Chukchi seas, the air temperatures were generally below −10°C except on March 11 and 13, when they rose to about −7°C. Before and after these dates, the air temperatures were well below −20°C. The wind speeds were less than 7 m/s and often less than 3 m/s. However, before March 17, both the air temperatures and wind measurements were obtained by hand-held instruments, so some inaccuracies in the measurements can be expected. From March 17 onward, an automated meteorological station was in place. Nevertheless, the air temperatures were not high enough for any moisture to be expected in the snow cover. The drift of the ice camp was determined by satellite positioning. On March 10 and 12 the drift speed rose rapidly to about 32 and 20 cm/s, respectively, due to winds of about 7 m/s. After March 14, the drift speed reduced to less than 5 cm/s as the wind decreased to less than 3 m/s. The day of the SAR overflight,

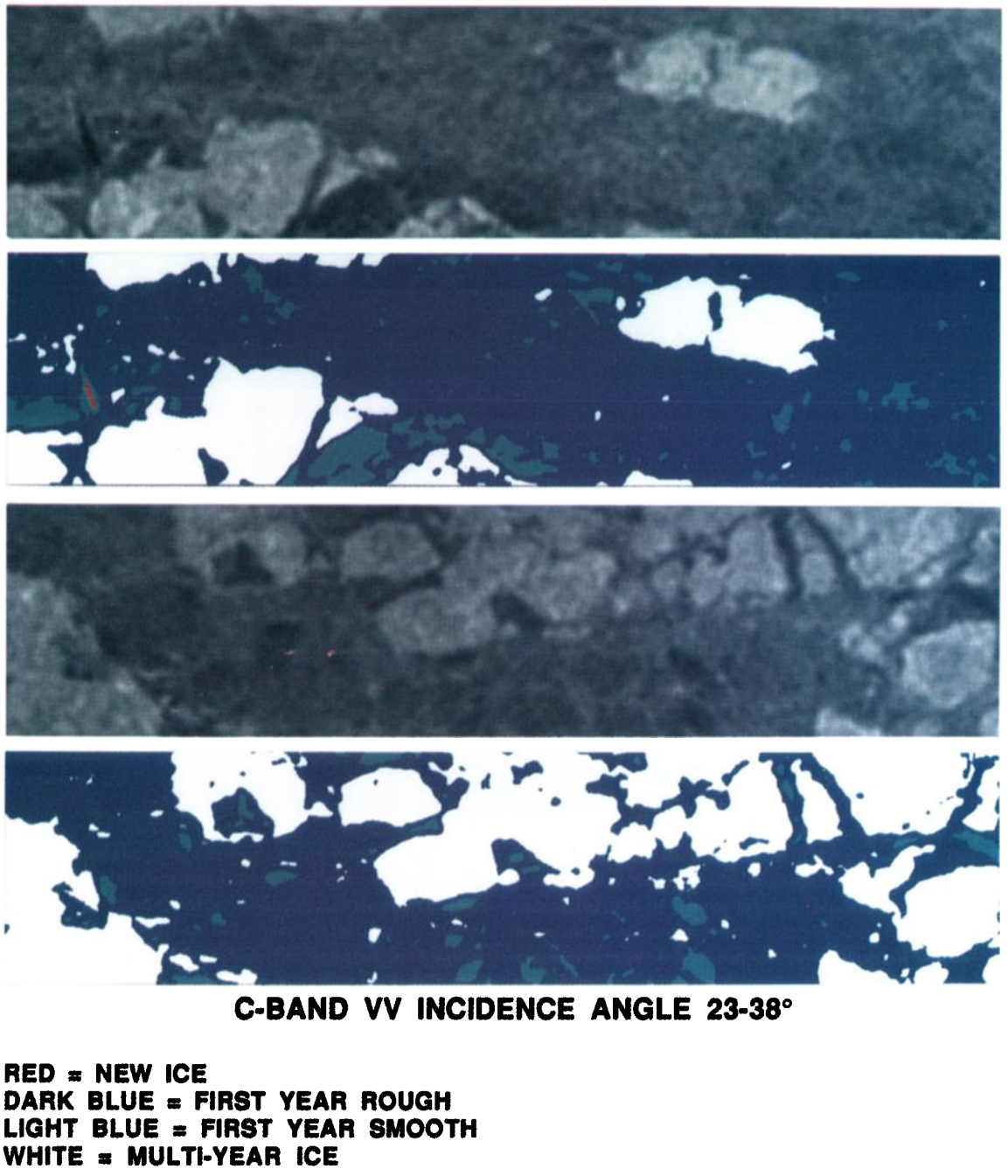

Plate 1. Classification maps of simulated 8 by 8 averaged ERS1 SAR data. White is multiyear ice; dark blue, smooth first-year ice; light blue, rough first-year ice; red, new ice/open water.

March 19, fell during a period of quiescence with little or no ice motion and air temperatures below −20°C, reducing the likelihood of open water being present in any recently opened leads.

Measurements of the sea ice in the area [*Wen et al.*, 1989] provide some key information on the understanding of the radar signatures in Plate 2. Most of the measurements were made of the refrozen lead rather than the multiyear floes. The lead was approximately 1.4 m thick and had a snow cover of about 15 cm, although the snow cover was unevenly distributed into sastrugi or windrows. The lead was surrounded by multiyear floes with a recently formed rubble field to the north containing large ice chunks. Fissures several centimeters in width were contained within the lead. Two ice cores were taken from the lead from which salinity, temperature, and density were measured and brine volume calculated (Figure 5). The ice was observed to be largely columnar in structure. Salinity profiles have values and a "C" shape characteristic of first-year ice of that thickness [*Weeks and Ackley*, 1982]. The temperature profiles are also characteristic of winter FY ice. No measurements of surface roughness of the ice and variable snow cover depth were made on the lead, but it is presumed to be relatively undeformed, since the lead was used as a landing strip and is referred to as "flat." The large multiyear floe where the ice camp was located was 6 by 6 km in size and contained hummocks as high as 6 m. In Plate 2, the ice camp was identified by knowledge of its location and by hand-held

photography and sketch maps of the camp itself [*Wen et al.*, 1989]. In the SAR image, the building of the camp appears as a bright point target situated on the less bright multiyear ice. Adjacent to the camp is the uniformly dark refrozen lead. These limited but important data enable exact identification of these two major ice types and provides an indication of the general ice types and conditions and corresponding signatures in the region. As can be seen in the classification image, the algorithm successfully delimits the MY and FY ice.

Comparison with KRMS data. During the March 1988 SSM/I validation, a K_a band scanning radiometer (KRMS) was flown along with the JPL SAR [*Cavalieri et al.*, 1991; *Eppler et al.*, 1986]. It provided some coincident coverage of the same ice fields. The passive microwave data were spatially registered to the SAR data for comparison of the active and passive signatures of the sea ice to assess the performance of the classification scheme. Plate 3 shows the coregistered SAR and KRMS data and their corresponding classification maps. The comparisons are admittedly more qualitative than quantitative owing to the lack of surface measurements in the area and also to the relative difficulty of geometrically registering the KRMS data to the SAR data (due to the poorer resolution performance of the KRMS). The KRMS data were also segmented into two regions, one corresponding to the brightness temperature of MY ice (white) and the other FY ice (dark). The MY fraction of each classified image was calculated and compared, the difference in the MY fraction between the two classification maps being less than 2%. Two other data sets comparing the classified KRMS data and SAR data acquired in the Beaufort have yielded comparable results.

The results are encouraging in that the ice type signatures derived from the limited SAR data set are similar to those in the scatterometer winter look-up table. If the signatures are stable as observed (under these winter conditions), then misclassification will be driven entirely by the computational aspects (segmentation) analyzed in section 2. This gives us an expected misclassification accuracy of less than 10%. However, it is quite difficult, as in most classification procedures, to state truly the expected accuracy of the classification map. The most important factor which affects classification accuracy is still the predictability of the physical variability of sea ice signatures.

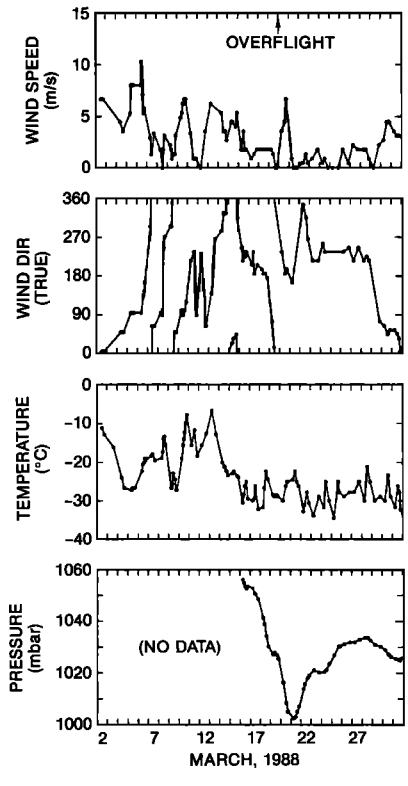

Fig. 4. Weather conditions at the ice camp [after *Wen et al.*, 1989].

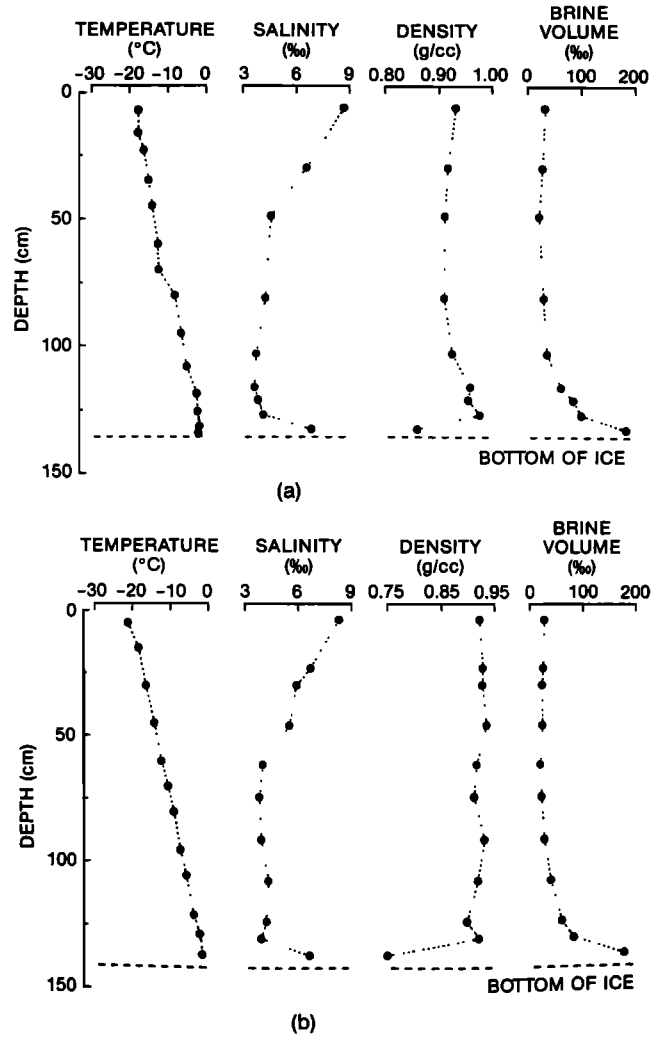

Fig. 5. Ice characteristics of two ice cores taken from a refrozen FY ice lead at the ice camp [*Wen et al.*, 1989].

5. Discussion

5.1. *Summary*

The classification approach and a subset of the simulation results obtained were presented in this paper. The dependence of the performance of the procedure on sea ice scattering characteristics and SAR system performance has been considered. The sensitivity of the procedure has also been analyzed.

The classification procedure worked well with the aircraft data set acquired over the Beaufort and Chukchi seas in March 1988. Comparison of the contrast observed in the SAR data and scatterometer measurements showed consis-

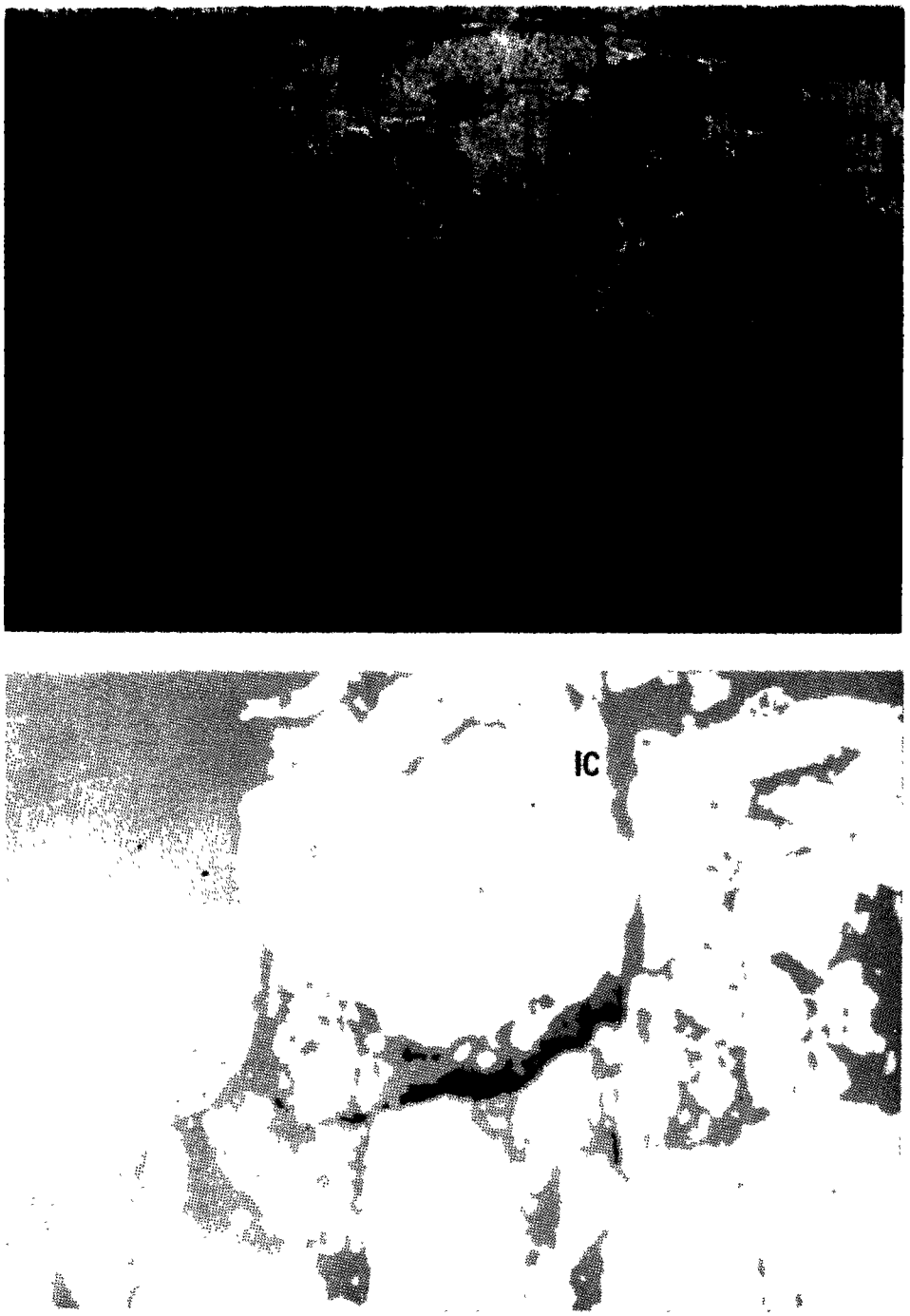

Plate 2. Aircraft SAR image of the ice camp area in the central Beaufort Sea (on March 19, 1988) and resulting classification. White is multi-year ice; grey, first-year ice; black, new ice/open water. IC denotes the position of the ice camp.

tency in the separation between MY and FY ice during this season. The discrimination of these two ice types is feasible under these winter Arctic conditions, although the detection of new ice and open water will probably be limited by system noise performance of the ERS-1 SAR. In the case of open water, the effect of wind on its scattering cross section will cause ambiguity in the intensity-based classification scheme suggested here. Also, the need for absolute and relative calibration of the radar data is demonstrated if our classification scheme is to be effectively mechanized. The effect of snow cover and surface melt conditions on scattering characteristics increases classification error. The look-up tables are designed to account for the influence of season and environmental conditions on the expected microwave behavior of sea ice. Scatterometer measurements have indicated that the contrast between FY and MY ice remains fairly stable for the period between October and May. The expected scattering behavior of sea ice during the spring, summer, and fall has also been described. We suggest that even though there is very little contrast between ice types, it is possible to discriminate between ice and open water during early, mid, and late summer. During the late spring

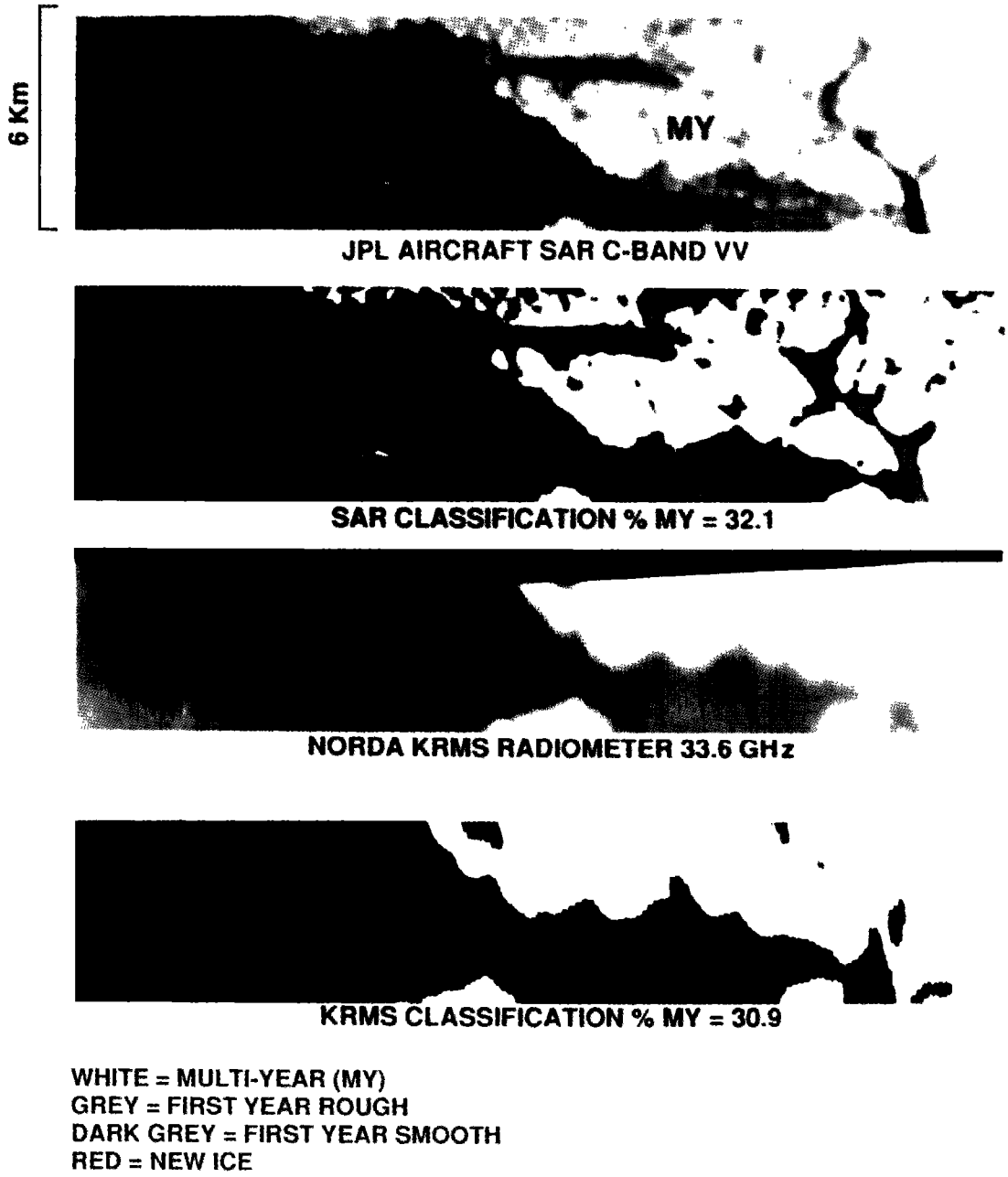

Plate 3. Comparison of classification results with KRMS data from March 11, 1988 in the central Beaufort Sea. White is multi-year ice; dark blue, smooth first-year ice; light blue, rough first-year ice; red, new ice/open water.

and fall it is possible to discriminate MY, FY, and open water/new ice although the contrast between these ice types will be slightly modulated by the moisture in the ice and snow. These effects are coded in the look-up tables constructed using scatterometer data. We anticipate that this classification algorithm will perform adequately during the winter and that further enhancements to the algorithm will be required during the specified seasons.

5.2. *Evolution of Approach and Postlaunch Validation*

It should be emphasized that this is an intensity-based classification scheme and that the use of other features (e.g., texture, higher-order moments, etc.) for ice classification has not been explored fully owing to lack of routine SAR observations required to understand and mechanize such schemes. Flexibility is designed into the classifier that these additional features and other measurements (passive microwave data) could be easily incorporated into the classification scheme. Also, the validity and confidence in the approach and the quality of the classification procedure will ultimately depend on an integrated program including field campaigns and aircraft underflights during the post-launch and operational phases to validate the approach as well as to provide ideas for improvement of this approach to ice classification. The approach suggested here should evolve with data available from routine coverage by ERS-1 in both the Arctic and Antarctic sea ice regions.

It is expected that these sea ice classification products

from SAR imagery will increase in value and utility after thorough validation is accomplished. Design changes and improvements will be required to incorporate the L band data from JERS-1 and RADARSAT imagery with its wide-swath capability. Obtaining extended time series by region and season will be extremely valuable for monitoring seasonal change, for heat flux calculations and for determining the role of the polar regions in global climate.

Acknowledgments. The authors wish to thank M. Drinkwater, J. Curlander, F. Carsey, and J. Crawford of JPL for their insightful suggestions, and D. Eppler and D. Farmer of NOARL at CRREL for the use of the KRMS imagery. This work was carried out under contract with the National Aeronautics and Space Administration at the Jet Propulsion Laboratory, California Institute of Technology.

REFERENCES

Alaska SAR Facility (ASF) Prelaunch Science Working Team, Science plan for the Alaska SAR Facility Program, *Publ. 89-14*, Jet Propul. Lab., Pasadena, Calif., 1989.

Ball, G. H., and D. J. Hall, A clustering technique for summarizing multi-variate data, *Behav. Sci.*, *12*, 153–155, 1967.

Burns, B. A., SAR image statistics related to atmospheric drag over sea ice, *IEEE Trans. Geosci. Remote Sens.*, *GE-28*(2), 158–165, 1990.

Burns, B. A., D. J. Cavalieri, M. R. Keller, W. J. Campbell, T. C. Grenfell, G. A. Maykut, and P. Gloersen, Multisensor comparison of ice concentration estimates in the marginal ice zone, *J. Geophys. Res.*, *92*(C7), 6843–6856, 1987.

Carsey, F. D., Summer Arctic sea ice character from satellite microwave data, *J. Geophys. Res.*, *90*(C3), 5015–5034, 1985.

Carsey, F., Review and status of remote sensing of sea ice, *IEEE J. Oceanic Eng.*, *OE-14*(2), 127–138, 1989.

Cavalieri, D. J., B. A. Burns, and R. G. Onstott, Investigation of the effects of summer melt on the calculation of sea ice concentration using active and passive microwave data, *J. Geophys. Res.*, *95*(C4), 5339–5369, 1990.

Cavalieri, D. J., J. P. Crawford, M. R. Drinkwater, D. T. Eppler, L. D. Farmer, R. R. Jentz, and C. C. Wackerman, Aircraft active and passive microwave validation of sea ice concentration from the Defense Meteorological Satellite Program special sensor microwave imager, *J. Geophys. Res.*, *96*(C12), 21,989–22,008, 1991.

Drinkwater, M. R., LIMEX '87 ice surface characteristics: Implications for C-band SAR backscatter signatures, *IEEE Trans. Geosci. Remote Sens.*, *GE-47*, 501–513, 1989.

Drinkwater, M., R. Kwok, D. Winebrenner, and E. Rignot, Multifrequency polarimetric SAR observations of sea ice, *J. Geophys. Res.*, *96*(C11), 20,679–20,698, 1991.

Eppler, D. T., L. D. Farmer, A. W. Lohanick, and M. Hoover, Classification of sea ice types with single band (33.6 GHz) airborne passive microwave imagery, *J. Geophys. Res.*, *91*(C9), 10,661–10,695, 1986.

Fily, M., and D. A. Rothrock, Opening and closing of sea ice leads: Digital measurements from synthetic aperture radar, *J. Geophys. Res.*, *95*(C1), 789–796, 1990.

Gray, A. L., R. K. Hawkins, C. E. Livingston, L. D. Arsenault, and W. M. Johnstone, Simultaneous scatterometer and radiometer measurements of sea-ice microwave signatures, *IEEE J. Oceanic Eng.*, *OE-7*(1), 20–32, 1982.

Hall, R. T., and D. A. Rothrock, Sea ice displacement from Seasat synthetic aperture radar, *J. Geophys. Res.*, *86*(C11), 11,078–11,082, 1981.

Holt, B., and S. A. Digby, Processes and imagery of first-year fast sea ice during the melt season, *J. Geophys. Res.*, *90*(C3), 5045–5062, 1985.

Holt, B., R. Kwok, and E. Rignot, Ice classification algorithm development and verification for the Alaska SAR Facility using aircraft imagery, in Proceedings of GARSS'89 Symposium, *IEEE Publ. 89CH2768-0*, pp. 751–754, Inst. of Electr. and Electron. Eng., New York, 1989.

Holt, B., R. Kwok, and J. Shimada, Ocean wave products from the Alaska SAR Facility Geophysical Processor System, in Proceedings of IGARSS'90 Symposium, *IEEE Publ. 90CH2825-8*, pp. 1469–1472, Inst. of Electr. and Electron. Eng., New York, 1990*a*.

Holt, B., R. Kwok, and E. Rignot, Status of the ice classification algorithm in the Alaska SAR Facility Geophysical Processor System, in Proceedings of IGARSS'90 Symposium, *IEEE Publ. 90CH2825-8*, pp. 2221–2224, Inst. of Electr. and Electron. Eng., New York, 1990*b*.

Kim, Y. S., R. K. Moore, R. G. Onstott, and S. Gogineni, Towards the identification of optimum radar parameters for sea-ice monitoring, *J. Glaciol.*, *31*(109), 214–219, 1985.

Kwok, R., J. C. Curlander, R. McConnell, and S. Pang, An ice motion tracking system at the Alaska SAR Facility, *IEEE J. Oceanic Eng.*, *OE-15*(1), 44–54, 1990.

Livingstone, C. E., and M. R. Drinkwater, Spring time C-band SAR backscatter signatures of Labrador Sea marginal ice: Measurements vs. modelling predictions, *IEEE Trans. Geosci. Remote Sens.*, *GE-29*(1), 29–41, 1991.

Livingstone, C. E., R. G. Onstott, L. D. Arsenault, A. L. Gray, and K. P. Singh, Microwave sea-ice signatures near the onset of melt, *IEEE Trans. Geosci. Remote Sens.*, *GE-25*(2), 174–187, 1987*a*.

Livingstone, C. E., K. P. Singh, and A. L. Gray, Seasonal and regional variations of active/passive microwave signatures of sea ice, *IEEE Trans. Geosci. Remote Sens.*, *GE-25*(2), 159–173, 1987*b*.

Lyden, J. D., B. Burns, and A. L. Maffet, Characterization of sea ice types using synthetic aperture radar, *IEEE Trans. Geosci. Electron.*, *GE-22*(5), 431–439, 1984.

Martin, S., B. Holt, D. J. Cavalieri, and V. Squire, Shuttle imaging radar-B (SIR-B) Weddell sea ice observations: A comparison of SIR-B and scanning multichannel microwave radiometer ice concentrations, *J. Geophys. Res.*, *92*(C7), 7173–7179, 1987.

Onstott, R. G., and S. P. Gogineni, Active microwave measurements of Arctic sea ice under summer conditions, *J. Geophys. Res.*, *90*(C3), 5035–5044, 1985.

Onstott, R., and R. A. Shuchman, Radar backscatter of sea ice during winter, in Proceedings of IGARSS '88 Symposium, *Eur. Space Agency Spec. Publ.*, *ESA SP-284*, vol. 2, 1115–1118, 1988.

Onstott, R. G., R. K. Moore, and W. F. Weeks, Surface-based scatterometer results of Arctic sea ice, *IEEE Trans. Geosci. Electron.*, *GE-17*(3), 78–85, 1979.

Onstott, R. G., R. K. Moore, S. Gogineni, and C. V. Delker, Four years of low altitude sea ice broadband backscatter measurements, *IEEE J. Oceanic Eng.*, *OE-7*(1), 44–50, 1982.

Onstott, R. G., T. C. Grenfell, C. Matzler, C. A. Luther, and E. A. Svendsen, Evolution of the microwave sea ice signatures during early summer and midsummer in the marginal ice zone, *J. Geophys. Res.*, *92*(C7), 6825–6835, 1987.

Tou, J., and R. Gonzalez, *Pattern Recognition*, Addison-Wesley, Reading, Mass., 1974.

Ulaby, F., R. K. Moore, and A. K. Fung, *Microwave Remote Sensing: Active and Passive*, vol. III, Artech House, Dedham, Mass., 1986.

Wackerman, C. C., R. R. Jentz, and R. A. Shuchman, Sea ice type classification of SAR imagery, in Proceedings of IGARSS '88 Symposium, *Eur. Space Agency Spec. Publ.*, *ESA SP-284*, vol. 2, 425–428, 1988.

Weeks, W. F., and S. F. Ackley, The growth, structure, and properties of sea ice, *CRREL Monogr. 82-1*, 130 pp., U.S. Army Cold Reg. Res. and Eng. Lab., Hanover, N. H., 1982.

Wen, T., W. J. Felton, J. C. Luby, W. L. J. Fox, and K. L. Kientz, Environmental measurements in the Beaufort Sea, Spring 1988, *Tech. Rep. ALP-UW TR 8822*, Appl. Phys. Lab., Univ. of Wash., Seattle, 1989.

Winebrenner, D. P., L. Tsang, B. Wen, and R. West, Sea-ice characterization measurements needed for testing of microwave remote sensing models, *IEEE J. Oceanic. Eng.*, *OE-14*(2), 149–157, 1989.

B. Holt, R. Kwok, and E. Rignot, Jet Propulsion Laboratory, 4800 Oak Grove Drive, Pasadena, CA 91109.

R. Onstott, Environmental Research Institute of Michigan, Ann Arbor, MI 48107.

(Received April 4, 1991;
revised August 17, 1991;
accepted September 30, 1991.)